Load Parameter Joint Identification of Wireless Power Transfer System Based on the DC Input Current and Phase-Shift Angle

Yanjie Guo, Yuwang Zhang, Shufan Li, Chengxuan Tao, *Member, IEEE*, and Lifang Wang, *Member, IEEE*

***Abstract*—This article presents a multiple load parameter joint identification method, adopting only the measured dc input current and inverter phase-shift angle of the wireless power transfer (WPT) system. First, a WPT fundamental–harmonic model is established, considering the effects of the battery and rectifier load. This model can quantitatively describe WPT characteristics and parameter relationships according to the linear superposition of fundamental and harmonic components. Then, the identification method is proposed through the model, which can achieve the joint identification of multiple important load parameters, including battery voltage, equivalent resistance, charging current, and WPT equivalent load impedance. Furthermore, on the basis of the developed WPT prototype, the effectiveness of the proposed fundamental–harmonic model is proved and the parameter sensitivity is discussed. Finally, the proposed identification method is experimentally studied, and the results show that it can achieve high accuracy on the conditions of battery voltage change, phase-shift angle variation, and coil misalignment.**

***Index Terms*—Harmonics, parameter identification, rectifier load, sensitivity, wireless power transfer (WPT).**

I. Introduction

WIRELESS power transfer (WPT) has become a highlight research topic and drawn more and more attention in recent years. WPT key issues have been deeply investigated, including coil optimization, compensation network design, power converter and control, etc., considering inductive power transfer, capacitive power transfer, and dynamic wireless power transfer [1]–[4].

One of the main WPT applications is charging batteries, such as the electric vehicle (EV) wireless charging. In these cases, wireless communication between the primary and secondary sides is usually adopted, which will increase the system cost and complexity [5], [6]. So, several parameter identification methods have been proposed to remove wireless communication based on the measured WPT primary-side variables [5]–[9]. In order to calculate the identified parameters, a WPT model is needed, which comprises coils [10], [11] and the compensation networks [12]–[14]. Furthermore, these two parts can be integrated together and expressed as a two-port network to simplify the calculations [15], [16]. Also, the inverter output is often equivalent to a voltage source [8], [12], and battery voltage or equivalent resistance is considered as the WPT load [8], [9], [17]. Through parameter relationships obtained from the WPT model [10], [18], load resistance and mutual inductance can be identified [5]–[7] and then used to implement the WPT system control [8], [9].

Moreover, the following four aspects will also affect the WPT parameter identification.

1) *Harmonic influence*: The inverter output voltage contains three, five, and other odd harmonics. Also, the harmonic components will change when adopting phase shifting, variable frequency pulsewidth modulation, and other control methods [19], [20]. These harmonics can be analyzed through nonlinear modeling or differential equations and will obviously affect the WPT characteristics in some cases [21], [22]. Since the traditional identification methods are based on the fundamental approximation [5]–[9], there will be some deviations when harmonics exist.
2) *Rectifier load*: The WPT equivalent load impedance can be adjusted to a pure resistance when adopting an active rectifier [23]. However, the uncontrolled diode rectifier is often used due to its simplicity and low cost. It can be described by the state-space model [24], and its input impedance contains both resistance and inductance parts [16]. Since the rectifier effect could lead to complex equations [25], only a resistance load is considered in most of the traditional identification methods [5], [6], [8], [9]. This cannot express the actual load features of the WPT system used for battery charging because the inductance part of the rectifier load will obviously affect the system power characteristics [16]. So, it will benefit high accuracy identification when adopting inductive equivalent load impedance.
3) *Battery dynamic process*: The battery parameters will change with the state-of-charge (SOC) during charging [26]. Typical battery parameters, such as voltage and

Manuscript received November 3, 2019; revised February 4, 2020; accepted March 9, 2020. Date of publication March 17, 2020; date of current version June 23, 2020. This work was supported by the National Key R&D Program of China under Grant 2018YFB0106300. Recommended for publication by Associate Editor M. Duffy. *(Corresponding author: Yanjie Guo.)*

The authors are with the Key Laboratory of Power Electronics and Electric Drives, Institute of Electrical Engineering, Chinese Academy of Sciences, Beijing 100190, China, and also with the University of Chinese Academy of Sciences, Beijing 100049, China (e-mail: yjguofa@163.com; zhangyuwang@mail.iee.ac.cn; lishufan@mail.iee.ac.cn; taochengxuan@mail.iee.ac.cn; wlf@mail.iee.ac.cn).

Color versions of one or more of the figures in this article are available online at http://ieeexplore.ieee.org.

Digital Object Identifier 10.1109/TPEL.2020.2981651

equivalent inter-resistance, can be identified based on the hybrid pulse power characteristic test [27]. When used for the WPT modeling, the battery is usually expressed as a voltage source or an equivalent resistance because of their simplicity and acceptable accuracy [8], [12], [17], [23], [28]. Also, the values of the voltage source and equivalent resistance will have dynamic processes varying with SOC during charging.

4) *System parameter variations*: Under actual WPT working conditions, coil misalignment may occur and lead to the coupling coefficient variation [29], [30]. Also, the phase-shift angle is adjusted for system control [28], [30]. These changes will affect the parameter identification process. Besides, there are some parameter microvariations in the WPT system [31]. For example, misalignment will also cause slight changes in coil self inductances. Sensitivity analysis can be conducted to study the effects of parameter changes [5], [7], [32], and the identification method should have good robustness when the WPT parameter microvariation happens.

Considering the above factors, a multiple load parameter joint identification method is proposed in this article. First, only the dc input current needed to be measured for parameter identification since phase-shift angle can be directly obtained from the controller. This will be easier to implement and also simplify the system, compared with the existing methods using the measured high-frequency ac variables [5]–[8], [33], [34]. Second, high accuracy can be achieved due to the established WPT fundamental–harmonic model and the quantitative description of the rectifier load. Third, the proposed identification method can achieve the joint identification of multiple important load parameters, including battery voltage, equivalent resistance, charging current, and WPT equivalent load impedance. This will benefit the system control, performance improvement, and system condition monitoring. Therefore, this article is organized as follows. Section II establishes the WPT fundamental and harmonic models. Section III proposes the load parameter identification method based on the dc input current and phase-shift angle. Section IV gives the experimental verifications and related discussions. Finally, Section V presents the conclusion.

II. System Modeling

Investigations, in this article, are based on the dual-side *LCC* compensation networks and the full-bridge diode rectifier, which are usually used for battery charging [12], [16]. Its topology is shown in Fig. 1(a), where the inverter consists of G_1–G_4, and the rectifier consists of D_1–D_4; compensation networks include L_p, L_s, C_{1s}, C_{1p}, C_{2s}, and C_{2p}; L_1, L_2, and M are, respectively, the self inductances of the transmit coil, receive coil, and mutual inductance between them; $C_{\rm in}$, C_o, and L_o are the system input and output filters; $U_{\rm dc}$ and $I_{\rm dc}$ are the dc source voltage and input current, respectively; U_b and I_b are the battery voltage and charging current, while U_b will vary with battery SOC during charging. Moreover, the dc source, input filter capacitor, and the inverter are treated as the WPT equivalent source. Additionally, the rectifier, output filter, and the battery are defined as the WPT equivalent load.

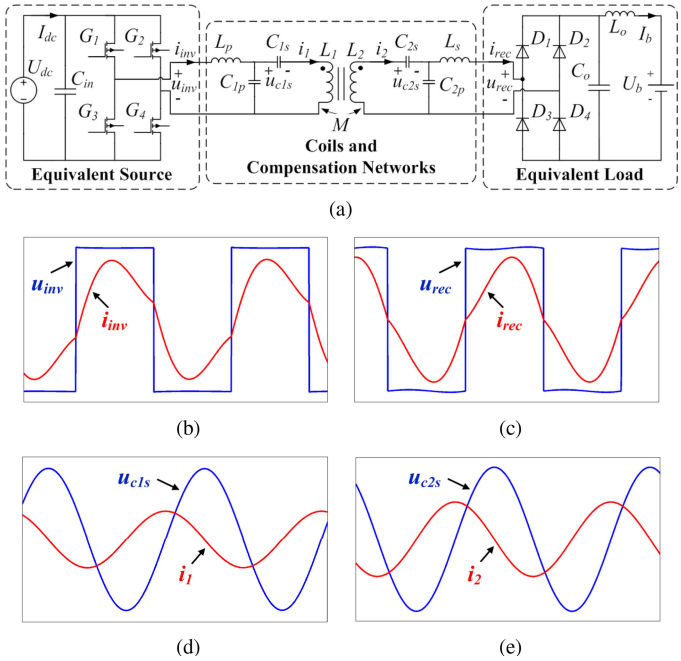

Fig. 1. WPT system and its typical waveforms. (a) WPT topology with *LCC* compensation networks and rectifier load for battery charging. (b) Schematic view of inverter output voltage $u_{\rm inv}$ and current $i_{\rm inv}$. (c) Schematic view of rectifier input voltage $u_{\rm rec}$ and current $i_{\rm rec}$. (d) Schematic view of primary-side voltage u_{c1s} and current i_1. (e) Schematic view of secondary-side voltage u_{c2s} and current i_2.

Furthermore, the typical waveforms of the WPT system are given in Fig. 1(b)–(e), where $u_{\rm inv}$ and $i_{\rm inv}$ are the inverter output voltage and current, respectively; $u_{\rm rec}$ and $i_{\rm rec}$ are the rectifier input voltage and current, respectively; i_1 and i_2 are the currents in the transmit and receive coils, respectively; u_{c1s} and u_{c2s} are the voltages on the compensation capacitors C_{1s} and C_{2s}, respectively; the detailed waveforms are obtained from the common working condition of the WPT system, as shown in Fig. 1(a). Also, only the case of rectifier continuous conduction mode (CCM) is considered because L_s needs to be big enough to avoid too large current peaks for safety. These figures suggest that the presented WPT system contains harmonics. In some parts, the harmonics are obvious, such as inverter output and rectifier input, while there is little harmonic in the other parts, for example, coil currents and series compensation capacitor voltages. According to the Fourier transform, the fundamental and harmonic components can be superimposed linearly, so they are going to be studied, respectively.

A. Fundamental Model

The WPT fundamental equivalent circuit is shown in Fig. 2, where $u_{\rm inv\_f}$ is the fundamental equivalent voltage source of inverter output; $i_{\rm inv\_f}$ is the fundamental inverter output current; R_1 and R_2 are the coil resistances; R_{Lp}, R_{Ls}, R_{1p}, R_{1s}, R_{2p}, and R_{2s} are the stray resistances of compensation networks; R_e and L_e are the WPT equivalent load impedance, which is the fundamental rectifier input impedance; u_{c2p} is the voltage on C_{2p}; and the fundamental rectifier input voltage and current are named $u_{\rm rec\_f}$ and $i_{\rm rec\_f}$. Also, the fundamental equivalent circuit is divided into three parts, according to Fig. 1(a).

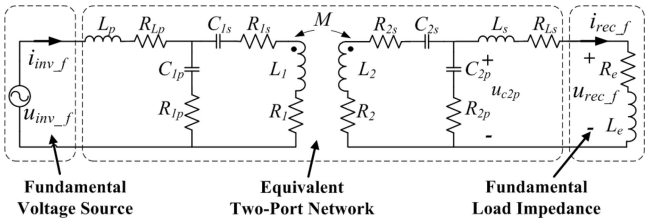

Fig. 2. WPT fundamental equivalent circuit and its components.

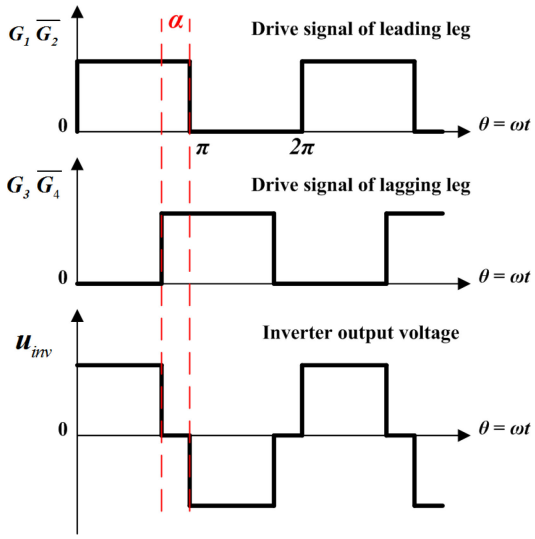

Fig. 3. Waveforms of inverter drive signals and output voltage to represent the phase-shift angle α.

First, the phase-shift control is usually used to regulate the WPT system [8], [28]. The related waveforms are shown in Fig. 3, where the phase-shift angle α is defined as the phase difference between the drive signals of the inverter leading leg and the lagging leg. The rms value of $u_{\mathrm{inv\_}f}$ is given by (1), where $U_{\mathrm{inv\_}f}$ is the fundamental rms value of $u_{\mathrm{inv\_}f}$. Since $u_{\mathrm{inv\_}f}$ is treated as the source, its phase angle is zero.

$$U_{\mathrm{inv\_}f} = \frac{2\sqrt{2}}{\pi} U_{\mathrm{dc}} \cos\frac{\alpha}{2}. \tag{1}$$

Then, the coils and compensation networks are equivalent to a two-port network [4], [15], [16], as shown in Fig. 2. Its impedance parameters are calculated and given by the following equation, where $Z_p = R_{Lp} + j\omega L_p$, $Z_s = R_{Ls} + j\omega L_s$, $Z_{1p} = R_{1p} + 1/j\omega C_{1p}$, $Z_{1s} = R_{1s} + 1/j\omega C_{1s}$, $Z_{2p} = R_{2p} + 1/j\omega C_{2p}$, $Z_{2s} = R_{2s} + 1/j\omega C_{2s}$, $Z_1 = R_1 + j\omega L_1$, $Z_2 = R_2 + j\omega L_2$, and $Z_m = j\omega M$; ω is the system angle frequency.

$$\begin{aligned} Z_{11} &= Z_p + \frac{Z_{1p}((Z_1+Z_{1s})(Z_2+Z_{2s}+Z_{2p}) - Z_m^2)}{(Z_1+Z_{1s}+Z_{1p})(Z_2+Z_{2s}+Z_{2p}) - Z_m^2} \\ Z_{12} &= Z_{21} = \frac{Z_{1p}Z_{2p}Z_m}{(Z_1+Z_{1s}+Z_{1p})(Z_2+Z_{2s}+Z_{2p}) - Z_m^2} \\ Z_{22} &= Z_s + \frac{Z_{2p}((Z_2+Z_{2s})(Z_1+Z_{1s}+Z_{1p}) - Z_m^2)}{(Z_1+Z_{1s}+Z_{1p})(Z_2+Z_{2s}+Z_{2p}) - Z_m^2}. \end{aligned} \tag{2}$$

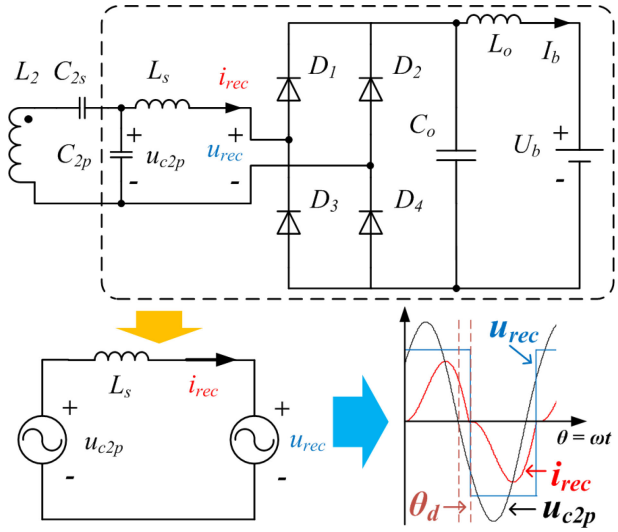

Fig. 4. Equivalent circuit and related schematic waveforms used to analyze the WPT equivalent load impedance.

Moreover, WPT equivalent load impedance R_e and L_e will be calculated. Fig. 1(c) indicates that the rectifier input voltage can be approximately described as a square wave and its amplitude is equal to the battery voltage U_b. Also, it is mainly affected by the rectifier-side circuit. On the other hand, the rectifier input current will be influenced by almost all WPT parameters, including source voltage, phase-shift angle, parameters of the coils and compensation networks, and rectifier-side circuit. Furthermore, R_e and L_e can be calculated through $u_{\mathrm{rec\_}f}$ and $i_{\mathrm{rec\_}f}$. But the results will be affected by almost all the WPT parameters, not only the rectifier-side circuit. In order to solve it, Fig. 4 presents the related equivalent circuit and schematic waveforms, where the equivalent circuit of WPT secondary side is shown; the part in the dashed box is simplified to get i_{rec} expression; positive zero crossing point of u_{rec} and i_{rec} is selected as the zero point of θ. Meanwhile, θ_d is defined in this figure, which is the phase angle difference between u_{c2p} and u_{rec}.

According to Fig. 4, the expression of the rectifier input current i_{rec} in the time domain is given by (3), where V_{c2p} is the amplitude of u_{c2p}. Also, the effects of R_{Ls}, diode resistances, and forward voltage drops are ignored here since u_{c2p} and u_{rec} are much bigger than the voltage drops on the stray resistances on WPT normal working conditions.

$$i_{\mathrm{rec}} = \begin{cases} \frac{1}{\omega L_s}\int_0^{\theta} (V_{c2p}\sin(\theta+\theta_d) - U_b)d\theta & 0 \le \theta < \pi \\ \frac{1}{\omega L_s}\int_{\pi}^{\theta} (V_{c2p}\sin(\theta+\theta_d) + U_b)d\theta & \pi \le \theta \le 2\pi. \end{cases} \tag{3}$$

As shown in Fig. 4, $i_{\mathrm{rec}} = 0$, when $\theta = \pi$. Also, charging current I_b is the average value of i_{rec} in the positive half cycle. Hence, the following relationships can be obtained:

$$\cos\theta_d = \frac{\pi U_b}{2V_{c2p}}, \quad \sin\theta_d = \frac{\pi\omega L_s I_b}{2V_{c2p}}. \tag{4}$$

On the basis of (3) and (4), i_{rec} fundamental Fourier coefficients a_1 and b_1 can be calculated and given by (5), according

to the Fourier transform

$$a_1 = \left(\frac{8}{\pi^2} - 1\right)\frac{\pi U_b}{2\omega L_s}, \quad b_1 = \frac{\pi I_b}{2}. \tag{5}$$

So, the amplitude and phase angle of $i_{\mathrm{rec\_}f}$ will be obtained from (6). Meanwhile, the amplitude and phase angle of $u_{\mathrm{rec\_}f}$ can be described as $|A_u| = 4U_b/\pi, \theta_u = -\pi/2$ since u_{rec} can be approximately treated as a square wave, as shown in Fig. 4

$$|A_i| = \sqrt{{a_1}^2 + {b_1}^2} = \frac{\pi}{2}\sqrt{\left(\frac{U_b}{\omega L_s}\left(\frac{8}{\pi^2} - 1\right)\right)^2 + {I_b}^2}$$

$$\tan\theta_i = -\frac{b_1}{a_1} = \frac{\omega L_s I_b}{U_b(1 - 8/\pi^2)}. \tag{6}$$

Furthermore, fundamental rectifier input impedance can be calculated through $u_{\mathrm{rec\_}f}$ divided by $i_{\mathrm{rec\_}f}$ in the frequency domain. Its expression is given in the following equation, according to the amplitudes and phase angles of $u_{\mathrm{rec\_}f}$ and $i_{\mathrm{rec\_}f}$:

$$R_e = \left|\frac{A_u}{A_i}\right|\cos(\theta_u - \theta_i) = \frac{8\omega^2 L_s^2 U_b I_b}{(\pi - 8/\pi)^2 U_b^2 + \pi^2\omega^2 L_s^2 I_b^2}$$

$$L_e = \left|\frac{A_u}{\omega A_i}\right|\sin(\theta_u - \theta_i) = \frac{8(1 - 8/\pi^2)L_s U_b^2}{(\pi - 8/\pi)^2 U_b^2 + \pi^2\omega^2 L_s^2 I_b^2}. \tag{7}$$

Also, the battery can be expressed as an equivalent resistance [23], [28], that is, $R_L = U_b/I_b$. Hence, the relationship between the WPT equivalent load impedance and R_L is given as

$$R_e = \frac{8\omega^2 L_s^2 R_L}{(\pi - 8/\pi)^2 R_L^2 + \pi^2\omega^2 L_s^2}$$

$$L_e = \frac{8(1 - 8/\pi^2)L_s {R_L}^2}{(\pi - 8/\pi)^2 R_L^2 + \pi^2\omega^2 L_s^2}. \tag{8}$$

Finally, the quantified expressions of the three parts of the WPT fundamental equivalent circuit have been obtained. Based on the established model, $i_{\mathrm{inv\_}f}$ and $i_{\mathrm{rec\_}f}$ are calculated and given by (9), where Z_e is the WPT equivalent load complex impedance, that is, $Z_e = R_e + j\omega L_e$. Besides, the fundamental components of other WPT voltages and currents can also be obtained through this model in similar ways

$$i_{\mathrm{inv\_}f} = \frac{2\sqrt{2}}{\pi}\frac{(Z_e + Z_{22})U_{\mathrm{dc}}}{Z_{11}(Z_e + Z_{22}) - Z_{12}Z_{21}}\cos\frac{\alpha}{2}$$

$$i_{\mathrm{rec\_}f} = \frac{2\sqrt{2}}{\pi}\frac{Z_{21}U_{\mathrm{dc}}}{Z_{11}(Z_e + Z_{22}) - Z_{12}Z_{21}}\cos\frac{\alpha}{2}. \tag{9}$$

B. Harmonic Model

In most of the existing design methods for the dual-side *LCC* compensation networks, C_{1s} and C_{1p} resonate with L_1, or they are not far from the resonance point. The WPT secondary side shares the same condition [12], [16]. So, the harmonic impedance of the branch of C_{1s} and L_1 will be significantly bigger than the one of the C_{1p} branch. Hence, we can think little harmonic flows through the branch of C_{1s} and L_1, and it can be treated as an open circuit to the harmonics. Also, the condition of the secondary side is similar. This conclusion is suitable for the WPT system well designed with *LCC* compensation networks. Therefore, as shown in Fig. 1(d) and (e), there are few harmonics in the voltages and currents of the coils and series compensation capacitors, which are not considered for the harmonic analysis. The WPT harmonic equivalent circuit is presented in Fig. 5, where the harmonic components of the inverter output voltage are treated as primary-side equivalent harmonic source $u_{\mathrm{inv\_}h}$; the harmonic components of the rectifier input voltage are described as secondary-side equivalent harmonic source $u_{\mathrm{rec\_}h}$; $i_{\mathrm{inv\_}h}$ and $i_{\mathrm{rec\_}h}$ are the harmonic inverter output and rectifier input currents.

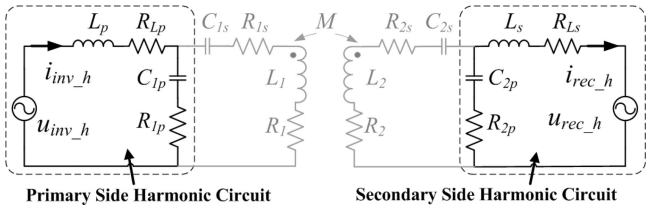

Fig. 5. WPT harmonic equivalent circuit and its parameters.

Fig. 5 suggests that the primary-side harmonics exist in the circuit composed of $u_{\mathrm{inv\_}h}$, primary-side compensation inductor, and parallel compensation capacitor, while the secondary-side harmonic circuit includes $u_{\mathrm{rec\_}h}$, secondary-side compensation inductor, and parallel compensation capacitor. In order to get harmonic expressions, the rms values of the harmonic voltage sources are given by the following equation, where $U_{\mathrm{inv\_}h}$ and $U_{\mathrm{rec\_}h}$ are the rms values of $u_{\mathrm{inv\_}h}$ and $u_{\mathrm{rec\_}h}$, respectively; k is the harmonic order:

$$U_{\mathrm{inv\_}h} = \frac{2\sqrt{2}}{k\pi}U_{\mathrm{dc}}\cos\frac{k\alpha}{2}, \quad U_{\mathrm{rec\_}h} = \frac{2\sqrt{2}}{k\pi}U_b. \tag{10}$$

Then, $i_{\mathrm{inv\_}h}$ and $i_{\mathrm{rec\_}h}$ can be calculated through the following equation, considering the impedances of the harmonic circuits:

$$i_{\mathrm{inv\_}h} = \frac{2\sqrt{2}}{k\pi}\frac{U_{\mathrm{dc}}\cos\frac{k\alpha}{2}}{(R_{Lp} + R_{c1p}) + j\left(k\omega L_p - \frac{1}{k\omega C_{1p}}\right)}$$

$$i_{\mathrm{rec\_}h} = -\frac{2\sqrt{2}}{k\pi}\frac{U_b}{(R_{Ls} + R_{c2p}) + j\left(k\omega L_s - \frac{1}{k\omega C_{2p}}\right)}. \tag{11}$$

Finally, the harmonic active power of the inverter output can be obtained from (12) and the WPT harmonic equivalent circuit model has been established. Based on this model, the harmonic components of other WPT voltages and currents can also be solved in similar ways, as well as the active and reactive powers

$$P_{h\_k} = \frac{\frac{8}{k^2\pi^2}U_{\mathrm{dc}}^2\cos^2\frac{k\alpha}{2}(R_{Lp} + R_{c1p})}{(R_{Lp} + R_{c1p})^2 + \left(k\omega L_p - \frac{1}{k\omega C_{1p}}\right)^2}. \tag{12}$$

To sum up, the WPT system characteristics and parameter relationships can be quantitatively studied based on the linear superposition of the fundamental and harmonic models. Also, the effects of battery and rectifier load are considered in the model. All these will benefit the high-accuracy analysis and the load parameter identification for the WPT systems.

III. Parameter Identification Method

There are several key load parameters in the WPT system. Battery voltage U_b is strongly related to the battery remaining power capacity [26], [27] and needs to be monitored for avoiding overcharging, as well as for battery state estimation. Meanwhile, U_b and charging current I_b are the common WPT controlled variables [8]. Their identification results will be helpful to the system control and performance improvement. Besides, battery equivalent resistance R_L has significant effect on the system characteristics [10], [18], and the WPT equivalent load impedance R_e and L_e are also important to the compensation network optimization [16]. The identification of these parameters will benefit the WPT condition monitoring. Therefore, considering all these load parameters, a joint identification method is proposed here, adopting only measured dc input current $I_{\rm dc}$ and obtained phase-shift angle α from the controller. Based on the presented fundamental–harmonic model, the detailed identification process is discussed as follows.

For the first step, battery equivalent resistance R_L is identified. Hence, we need to find the relationship between R_L and $I_{\rm dc}$. Considering the fundamental circuit, first, the inverter fundamental output impedance is given by the following equation, where $Z_{\rm rec\_f}$ is calculated through equivalent two-port network and WPT equivalent load impedance; and $R_{\rm rec\_f}$ and $L_{\rm rec\_f}$ are the fundamental equivalent resistance and inductance of the inverter output, respectively:

$$Z_{\rm inv\_f} = Z_{11} - \frac{Z_{12}Z_{21}}{Z_e + Z_{22}} = R_{\rm inv\_f} + j\omega L_{\rm inv\_f}. \tag{13}$$

Then, the relationship between the WPT dc input side and the inverter output side is obtained; based on that, the inverter output active power is approximately equal to the WPT dc input power on the assumption of ignoring inverter power loss. This can be established as follows, where P_f is the fundamental inverter output active power:

$$P_f + \sum_{k=3}^{n} P_{h\_k} \approx U_{\rm dc} I_{\rm dc}. \tag{14}$$

According to (1), (12), and (13), the expressions of the fundamental and harmonic inverter output active powers can be given by (15), where fundamental impedance factor β_f and harmonic impedance factor β_h are defined for simplifying. As suggested by (8) and (13), β_f is related to R_L, while β_h is constant, when considering the specific order harmonic.

$$\begin{cases} P_f = \frac{8}{\pi^2}\frac{R_{\rm inv\_f}}{{R_{\rm inv\_f}}^2+\omega^2{L_{\rm inv\_f}}^2}U_{\rm dc}^2\cos^2\frac{\alpha}{2} = \frac{8}{\pi^2}\beta_f U_{\rm dc}^2\cos^2\frac{\alpha}{2} \\ P_{h\_k} = \frac{\frac{8}{k^2\pi^2}U_{\rm dc}^2\cos^2\frac{k\alpha}{2}(R_{Lp}+R_{c1p})}{(R_{Lp}+R_{c1p})^2+\left(k\omega L_p-\frac{1}{k\omega C_{1p}}\right)^2} = \frac{8}{k^2\pi^2}\beta_h U_{\rm dc}^2\cos^2\frac{k\alpha}{2}. \end{cases} \tag{15}$$

So, the approximate relationship between the inverter output active power and WPT dc input power can be given by

$$\frac{8}{\pi^2}\beta_f {U_{dc}}^2\cos^2\frac{\alpha}{2} + \sum_{k=3}^{n}\frac{8}{k^2\pi^2}\beta_h {U_{dc}}^2\cos^2\frac{k\alpha}{2} \approx U_{\rm dc} I_{\rm dc}. \tag{16}$$

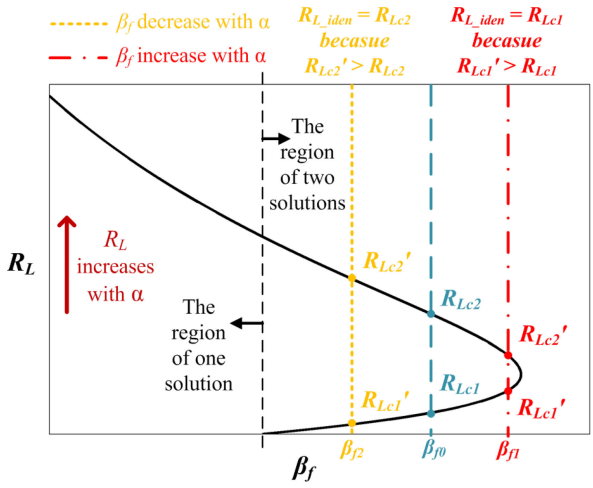

Fig. 6. Schematic view of the relationship between R_L and β_f, as well as α influence.

On the basis of (16), the relationship between β_f and $I_{\rm dc}$ is given by (17). Since the phase-shift angle α will be easily obtained from the inverter controller, it could be thought of as a known parameter here. Hence, β_f can be calculated according to the measured $I_{\rm dc}$

$$\beta_f = \frac{1}{\cos^2\frac{\alpha}{2}}\left(\frac{\pi^2 I_{\rm dc}}{8U_{\rm dc}} - \sum_{k=3}^{n}\frac{\beta_h}{k^2}\cos^2\frac{k\alpha}{2}\right). \tag{17}$$

Furthermore, the relationship between R_L and β_f is discussed, which is defined by (2), (8), (13) and (15). Equations (13) and (15) indicate that the function of R_L and β_f essentially reflects the relationship between R_L and fundamental active power of the inverter output. So, there will be a peak in the $\beta_f - R_L$ curve, which is the same with the case between the load resistance and WPT transferred power [10], [18]. According to this relationship, the schematic view of the $\beta_f - R_L$ curve is shown in Fig. 6. Moreover, the relationship between β_f with $I_{\rm dc}$ will only be affected by α when the WPT system has been finished for design and used in practice, as suggested by (17). So, α influence is also given in the figure in order to provide a clear understanding and an overall explanation of the parametric relationships, where the case β_f decreases with α and is presented with a yellow dotted line; the case β_f increases with α and is shown with a red dotted dash line.

Fig. 6 suggests that in the region of one solution, the identified battery equivalent resistance $R_{L\_\rm iden}$ is directly equal to the calculated result R_{Lc}. In the region of two solutions, there will be two calculated results R_{Lc1} and R_{Lc2} ($R_{Lc1} < R_{Lc2}$), and the right one needs to be distinguished. Considering increasing phase-shift angle α, this will affect measured $I_{\rm dc}$ and then impact β_f. Whether β_f increases or decreases, one calculated R_L result will increase and the other one will reduce. However, α increasing will bring the decreasing of the system output power. So, charging current I_b will reduce since α adjustment time is short and battery voltage U_b can be thought constant. This will bring the increasing of R_L. Hence, the increasing one will be the right calculated R_L result, when α becomes larger.

Based on the above analysis, the R_L identification process in the two solution region can be described as follows: First, increase α, if there is only one new calculated R_L result, $R_{L\_\mathrm{iden}} = R_{Lc2}$. The other case is that there are two new calculated results R'_{Lc1} and R'_{Lc2} ($R'_{Lc1} < R'_{Lc2}$). So, $R_{L\_\mathrm{iden}} = R_{Lc1}$, when $R'_{Lc1} > R_{Lc1}$; and $R_{L\_\mathrm{iden}} = R_{Lc2}$, when $R'_{Lc1} < R_{Lc1}$, as shown in Fig. 6. Up to now, the first step is completed and R_L is identified through the measured I_{dc} by introducing the intermediate variable β_f.

For the second step, the identification results of the WPT equivalent load impedance R_{e_iden} and L_{e_iden} can be obtained from (8) based on R_{L_iden}.

For the third step, battery voltage U_b is identified. First, the identification result of the fundamental inverter output current $i_{\mathrm{inv}\_f\_\mathrm{iden}}$ can be obtained by (9), according to R_{e_iden}, L_{e_iden}, and the measured system parameter values. Then, the transfer function between the fundamental rectifier input voltage and inverter output current is calculated and given by the following equation according to the established WPT fundamental model and the equivalent two-port network, where $Z_{e\_\mathrm{iden}} = R_{e\_\mathrm{iden}} + j\omega L_{e\_\mathrm{iden}}$:

$$G_u = \frac{u_{\mathrm{rec}\_f}}{i_{\mathrm{inv}\_f}} = \frac{Z_{e\_\mathrm{iden}} Z_{21}}{Z_{e\_\mathrm{iden}} + Z_{22}}. \tag{18}$$

Finally, U_b identification result can be obtained from the following equation based on the relationship between the amplitude of the rectifier input voltage and its fundamental rms value:

$$U_{b\_\mathrm{iden}} = \frac{\pi}{2\sqrt{2}} \left| G_u i_{\mathrm{inv}\_f\_\mathrm{iden}} \right|. \tag{19}$$

For the fourth step, charging current I_b is identified. First, the fundamental inverter output current is identified through (9), which is the same as the U_b identification process.

Then, the transfer function between the fundamental rectifier input current and inverter output current is calculated and given by

$$G_i = \frac{i_{\mathrm{rec}\_f}}{i_{\mathrm{inv}\_f}} = \frac{Z_{21}}{Z_{e\_\mathrm{iden}} + Z_{22}}. \tag{20}$$

On the basis of (20), the fundamental amplitude and phase angle of rectifier input current i_{rec} will be obtained. Moreover, the harmonic amplitudes and phase angles of i_{rec} are obtained through (11) based on the presented WPT harmonic model. Therefore, i_{rec} can be calculated according to the linear superposition of its fundamental and harmonic components.

Finally, I_b identification result is obtained from the following equation, considering that I_b is the average value of i_{rec} in the positive half cycle, where A_{ir1} and θ_{ir1} are the fundamental amplitude and phase angle of i_{rec}, respectively; and A_{irk} and θ_{irk} are the harmonic amplitudes and phase angles, respectively:

$$\begin{aligned} I_{b\_\mathrm{iden}} &= \frac{1}{\pi} \int_0^{\pi} \left(A_{ir1} \sin(\theta + \theta_{ir1}) + \sum_{k=3}^{n} A_{irk} \sin(k\theta + \theta_{irk}) \right) d\theta \\ &= \frac{2}{\pi} A_{ir1} \cos\theta_{ir1} + \sum_{k=3}^{n} \frac{2}{k\pi} A_{irk} \cos\theta_{irk}. \end{aligned} \tag{21}$$

To sum up, the process of the proposed multiple load parameters identification method is shown in the flowchart in Fig. 7. This method can achieve the joint identification of several key WPT load parameters. Also, it is easy to be implemented since only the dc input current is measured for identification.

IV. Experimental Verification and Discussion

A. WPT Prototype and Parameter Values

A WPT prototype, as shown in Fig. 8, is developed to verify the proposed model and the load parameter identification method. Its configuration is the same as the WPT topology, as presented in Fig. 1(a). A dc voltage source is adopted as the system power source. The full-bridge single-phase inverter is composed of SiC MOSFETs with the type C3M0065090D. The full-bridge rectifier is composed of SiC diodes with the type C3D16060D. Also, the input dc voltage is set to 350 V and the system operating frequency is 85 kHz.

The transmit coil is a rounded rectangle with size 58 cm $\times$ 42 cm, and the receive coil is a square with size 32 cm $\times$ 32 cm. The vertical distance between them is 20 cm. The detailed parameter values of the coils and compensation networks have been listed in Table I, as well as the system power level. Additionally, there are some parasitic parameters existing in the prototype. A part of their disturbance can be eliminated through the high-accuracy parameter measurement based on the practical devices. As presented in Table I, the parasitic inductances and resistances are included in the measurement results. Consideration of the other part of their disturbance is related to sensitivity and will be discussed in Section IV-C.

The electric load works in the constant voltage mode to simulate the battery-type load. Moreover, the tested voltages of a $LiFePO_4$ power battery used for EVs are given in Fig. 9. It suggests that the battery voltage will change with SOC and the range is from 300 to 360 V during most of the charging time. So, this voltage change range is adopted in the electric load for the following experiments and analysis.

B. System Model Verification

Based on the prototype, the proposed fundamental–harmonic model is verified and the results are shown in Fig. 10, where i_{inv} and i_{rec} are taken as the examples; the calculated results are obtained from the model in Section II, considering three-, five-, and seven-order harmonics. Also, different battery voltages and phase-shift angles are adopted for better verification.

Fig. 10 indicates that there are some deviations between the calculated and experimental results. They are caused by the ignoring of the converter nonideal process as well as the stray parameters. Meanwhile, higher harmonics than the seventh may also affect the waveform details. However, the calculated waveforms are very close to the experimental ones. So, the proposed model has been verified, and the results show that it can achieve high accuracy on the conditions of different battery voltages and phase-shift angles.

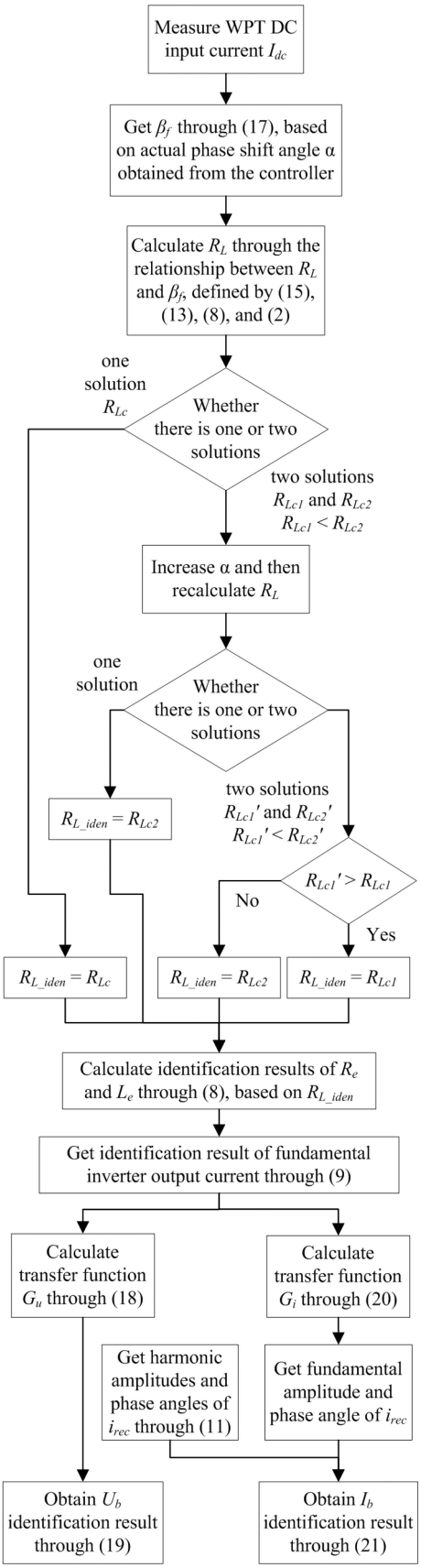

Fig. 7. Flowchart of the proposed multiple load parameter joint identification method based on the WPT dc input current and inverter phase-shift angle.

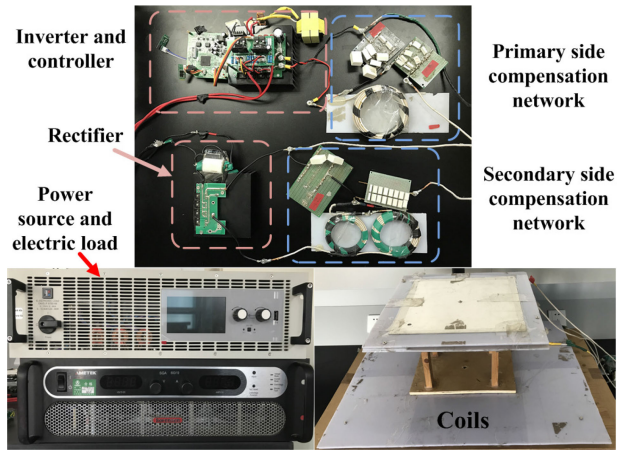

Fig. 8. Photograph of the developed WPT prototype.

TABLE I
PARAMETER VALUES OF THE DEVELOPED WPT PROTOTYPE

Parameters	Values
L_1, L_2, M	235.69 μH, 214.11 μH, 25.79 μH
L_p, L_s	80.30 μH, 84.10 μH
C_{1s}, C_{1p}, C_{2s}, C_{2p}	18.72 nF, 82.90 nF, 24.22 nF, 67.58 nF
R_1, R_2, R_{Lp}, R_{Ls}	217 mΩ, 223 mΩ, 115 mΩ, 124 mΩ
Power level	2 kW

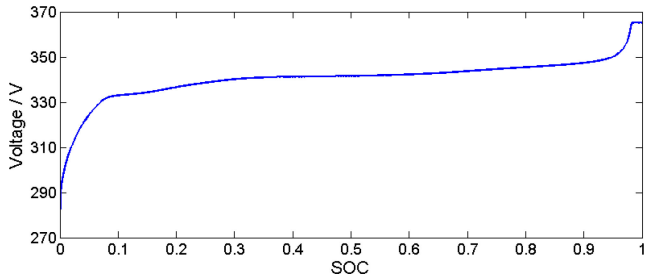

Fig. 9. Tested voltage values of a $LiFePO_4$ battery when SOC changes.

C. Investigation of Parameter Sensitivity

Parameter sensitivity will affect the performance of the identification method, due to that the WPT parameters may vary in practice [30], [32]. Here, the relationship between $I_{\rm dc}$ and R_L is selected as the example since it is the basis of the proposed identification method; d is defined as the misalignment distance. Also, because the parameter microvariations will occur [31], we choose the slight change of coil self-inductance L_1 to show the influence, considering its variation during misalignment.

First, the parameter sensitivity is analyzed in theory through the derivative [5], [7], [32]. Equation (17) is used to study the sensitivity of the proposed method to phase-shift angle α because the effect of α is mainly reflected in this equation. The calculation result is given by (22). It suggests that this derivative is significantly affected by α. So, the $I_{\rm dc} - R_L$ relationship is

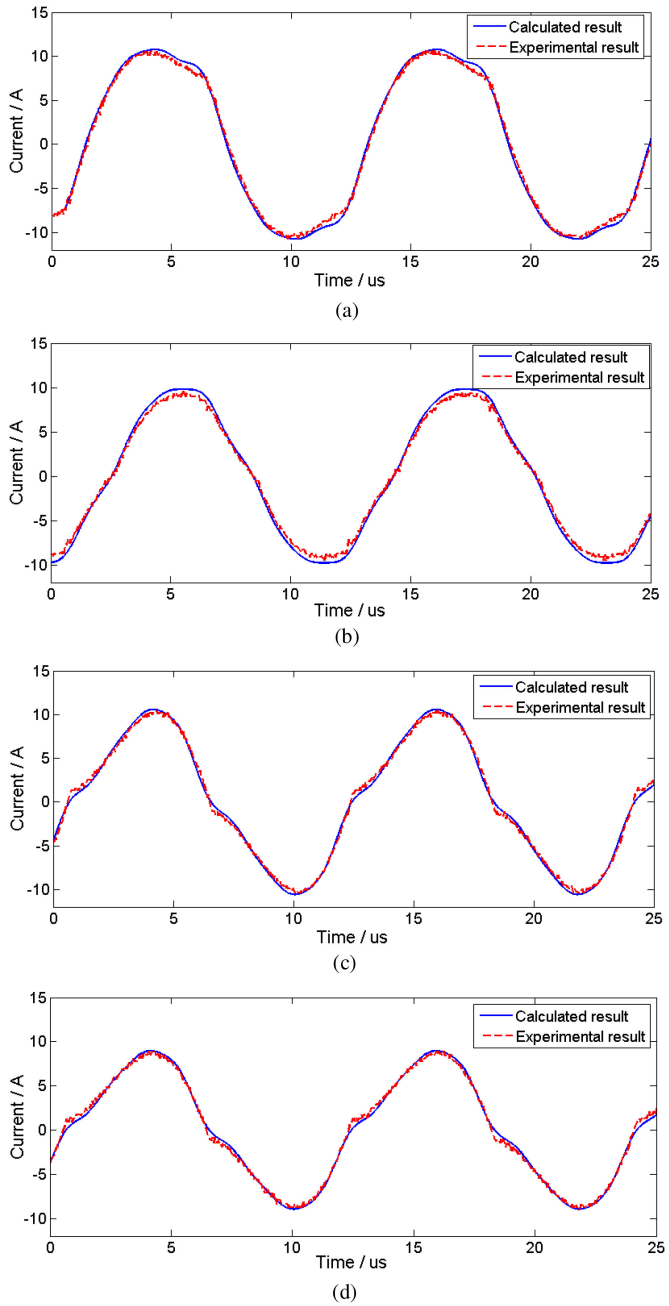

Fig. 10. Experimental verifications of the proposed WPT fundamental–harmonic model through the measured current waveforms. (a) i_{inv} results on the condition of $U_b = 360$ V and $\alpha = 0°$. (b) i_{inv} results on the condition of $U_b = 300$ V and $\alpha = 60°$. (c) i_{rec} results on the condition of $U_b = 360$ V and $\alpha = 0°$. (d) i_{rec} results on the condition of $U_b = 300$ V and $\alpha = 60°$.

very sensitive with phase-shift angle α.

$$\frac{d\beta_f}{d\alpha} = \frac{\sin\frac{\alpha}{2}}{\cos^3\frac{\alpha}{2}}\left(\frac{\pi^2 I_{\mathrm{dc}}}{8U_{\mathrm{dc}}} - \sum_{k=3}^{n}\frac{\beta_h}{k^2}\cos^2\frac{k\alpha}{2}\right) + \frac{1}{\cos^2\frac{\alpha}{2}}\left(\sum_{k=3}^{n}\frac{\beta_h}{k}\cos\frac{k\alpha}{2}\sin\frac{k\alpha}{2}\right). \quad (22)$$

Then, the sensitivity of the proposed method to L_1 microvariation is studied based on the impedance factors A and B defined in the following equation to simplify the expressions:

$$A = Z_1 + Z_{1s} + Z_{1p}$$
$$B = Z_2 + Z_{2s} + Z_{2p}. \quad (23)$$

So, Z_{11} expression can be simplified as the following, based on (2):

$$Z_{11} = Z_p + Z_{1p} - \frac{{Z_{1p}}^2 B}{AB + \omega^2 M^2}. \quad (24)$$

When L_1 has microvariation, there will be a small change of Z_1, which is defined as ΔZ_1. Hence, Z_{11} after L_1 microvariation is named ${Z_{11}}'$ and its expression is given by

$${Z_{11}}' = Z_p + Z_{1p} - \frac{{Z_{1p}}^2 B}{(A + \Delta Z_1)B + \omega^2 M^2}. \quad (25)$$

Therefore, the difference between Z_{11} and ${Z_{11}}'$ is calculated and given by

$$Z'_{11} - Z_{11} = \frac{Z_{1p}^2 B^2}{AB + \omega^2 M^2}\frac{1}{\frac{AB+\omega^2M^2}{\Delta Z_1} + B}. \quad (26)$$

As mentioned in Section II-B, C_{1s} and C_{1p} resonate with L_1, and they are not far from the resonance point. C_{2s}, C_{2p}, and L_2 share the same condition. So, the impedance factors A and B will be small since the stray resistances of the coils and compensation networks are relatively small. Hence, the difference between Z_{11} and ${Z_{11}}'$ can be approximately expressed by

$$Z'_{11} - Z_{11} \approx \frac{Z_{1p}^2 B^2}{(AB + \omega^2 M^2)^2}\Delta Z_1. \quad (27)$$

Since B is much smaller than $\omega^2 M^2$ and ΔZ_1 is only a small change caused by L_1 microvariation, the value of this difference is small. This means Z_{11} will not be much affected by L_1 microvariation. There will be similar conclusions with the other parameters of the equivalent two-port network. So, the $I_{\mathrm{dc}} - R_L$ relationship is not sensitive with the L_1 microvariation because L_1 mainly affects this relationship through the equivalent two-port network parameters. Therefore, good robustness can be achieved when the WPT parameter microvariation happens, according to the theoretical analysis based on the example of L_1 microvariation. Besides, some parameter microvariations are caused by the uncertain parasitic parameters. Their influences can be theoretically studied in a similar way to demonstrate that the proposed method has good robustness in these cases.

Furthermore, parameter sensitivity is investigated based on the actual parameter values of the developed WPT prototype and the results are shown in Fig. 11. It suggests the $I_{\mathrm{dc}} - R_L$ relationship is very sensitive with phase-shift angle α, which is the same with the conclusion of the theoretical analysis. Hence, the actual α value needs to be obtained from the controller when the phase-shift control is conducted. Fig. 11(b) shows that coil mutual inductance M also has an obvious effect on the $I_{\mathrm{dc}} - R_L$ relationship. Since an auxiliary positioning device can be used in some typical applications, such as the EV wireless charging, the value of M could be obtained from this kind of device and updated for parameter identification. However, an auxiliary positioning device will increase the cost, complexity,

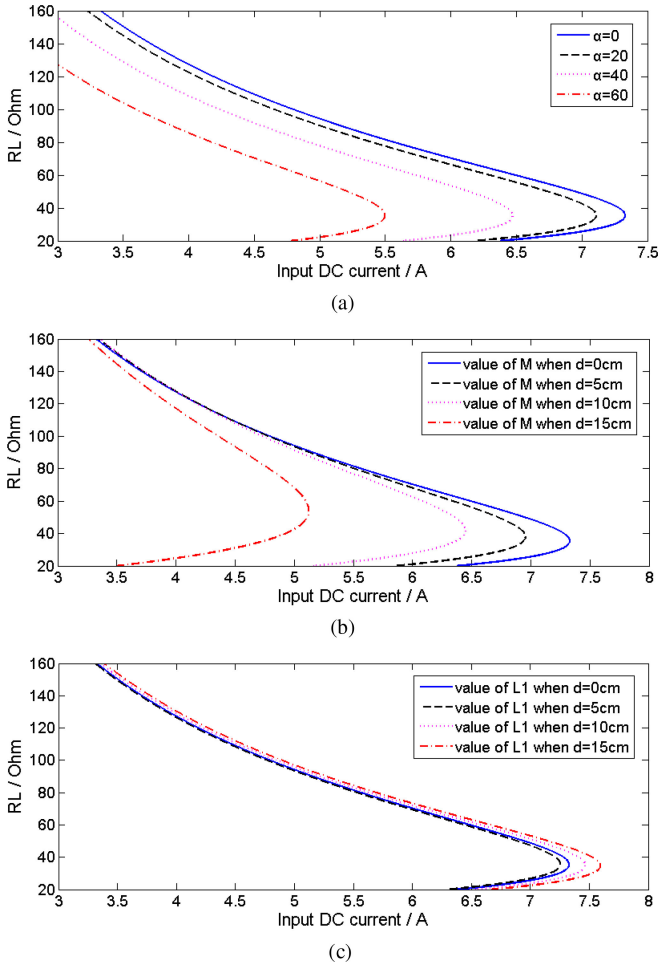

Fig. 11. Parameter sensitivity analysis considering the influence of dc input current $I_{\rm dc}$ on battery equivalent resistance R_L. (a) Case that α changes. (b) Case that M changes. (c) Case that L_1 has microvariation.

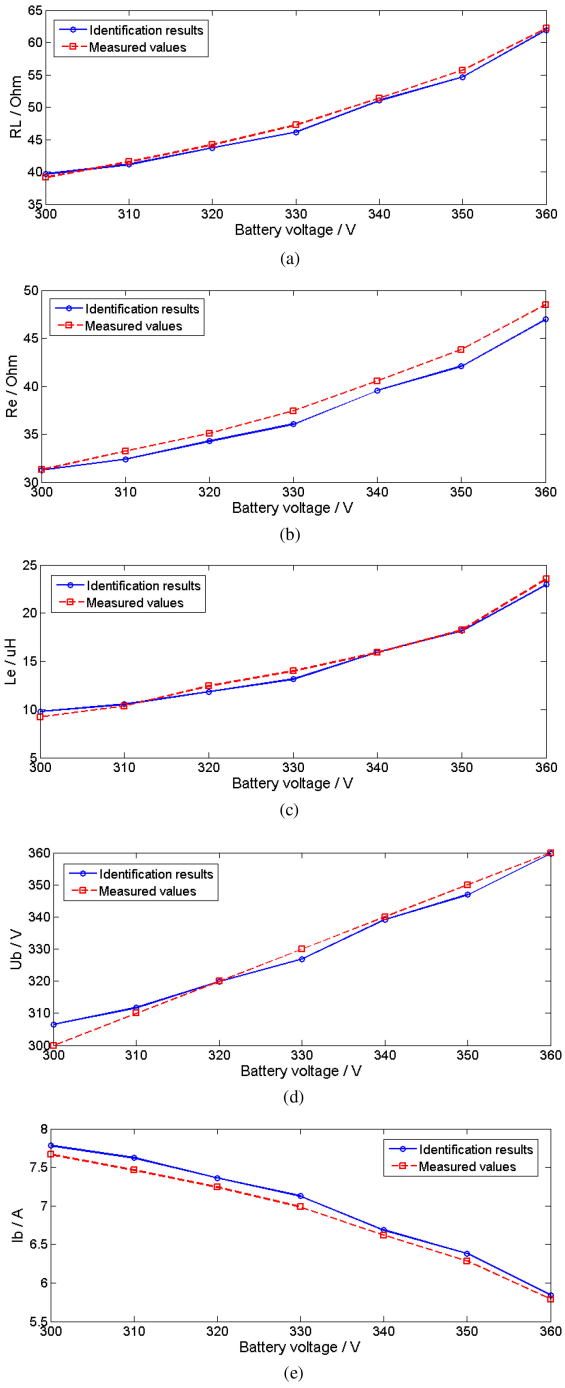

Fig. 12. Load parameter identification results when the battery voltage changes with SOC. (a) R_L identification results. (b) R_e identification results. (c) L_e identification results. (d) U_b identification results. (e) I_b identification results.

and inaccuracy of the proposed method in practicality. Hence, a mutual-inductance identification algorithm will be added to the method in future research to solve this problem. Fig. 11(c) indicates that there are only small changes of $I_{\rm dc} - R_L$ relationship, considering the L_1 microvariation, which is also consistent with the theoretical analysis result. So, the proposed load parameter identification method will have good robustness when the WPT parameter microvariation occurs.

D. Parameter Identification Method Analysis

In the practical charging process, the battery voltage changes with SOC [26], [27], which will lead to the dynamic variations of the battery equivalent resistance and the WPT equivalent load impedance. Meanwhile, the phase-shift angle can be adjusted to implement the control strategies [28], [30]. Also, there may be some variations of the coupling coefficient [29], [30] due to the coil position change, such as the misalignment condition. So, the proposed multiple load parameter joint identification method is verified and discussed, considering the above three aspects.

First, the case of the battery voltage change is considered and the results are shown in Fig. 12, where the measured results of R_e and L_e are obtained through the fast Fourier transform of the experimental waveforms; three-, five-, and seven-order harmonics are considered to obtain the experimental identification results. Further calculations indicate that the maximum identification errors of R_L, U_b, and I_b are 2.3%, 2.2%, and 2.2%, respectively, while the maximum difference between the identified and measured R_e is 1.7 Ω, and the one of L_e is 0.85 μH. These errors are mainly caused by the measure deviations of parameter values

TABLE II
IDENTIFICATION RESULTS OF WPT EQUIVALENT LOAD IMPEDANCES ON THE CONDITION OF DIFFERENT PHASE-SHIFT ANGLES

Experimental Parameter Values		Identified Equivalent Load		Experimental Equivalent Load	
U_b (V)	α (Degree)	R_{e_iden} (Ω)	L_{e_iden} (uH)	R_e (Ω)	L_e (uH)
300	0	31.25	9.78	31.29	9.23
	20	31.96	10.24	32.13	9.66
	40	35.82	12.97	36.01	12.87
	60	45.23	21.17	45.45	20.70
360	0	46.98	22.96	48.51	23.54
	20	47.68	23.71	48.73	23.83
	40	55.81	33.46	58.07	32.76
	60	78.49	76.13	89.32	77.81

TABLE III
IDENTIFICATION RESULTS OF BATTERY VOLTAGES, EQUIVALENT RESISTANCES, AND CHARGING CURRENTS ON THE CONDITION OF DIFFERENT PHASE-SHIFT ANGLES

Experimental Parameter Values		Identified Battery Voltage	Measured and Identified Battery Equivalent Resistance		Measured and Identified Charging Current	
U_b (V)	α (Degree)	U_{b_iden} (V)	R_L (Ω)	R_{L_iden} (Ω)	I_b (A)	I_{b_iden} (A)
300	0	306.48	39.13	39.63	7.67	7.78
	20	305.05	40.23	40.58	7.46	7.57
	40	306.26	45.27	45.84	6.63	6.72
	60	307.54	58.09	59.28	5.16	5.22
360	0	359.68	62.20	61.90	5.79	5.84
	20	355.78	62.83	62.97	5.73	5.68
	40	354.19	76.40	75.91	4.71	4.69
	60	348.91	128.94	122.82	2.79	2.86

and experimental waveforms, as well as some approximations in the modeling process. But these errors and differences are relatively small, so the proposed parameter identification method can achieve high accuracy on the condition of the battery load dynamic change.

Then, the condition of the different phase-shift angles is studied and the results are given in Tables II and III, where the phase-shift angle range is selected as 0°–60°, in order to make the WPT system working in the rectifier CCM state during most of the battery voltage variations. The results in these two tables indicate that some identification errors are relatively big in the case of $U_b = 360$ V and $\alpha = 60°$. This is due to the rectifier discontinuous conduction mode, which is out of the scope of this article. In other cases, the maximum errors of R_L, U_b, and I_b are 2.0%, 2.5%, and 1.5%, respectively, while the maximum difference between the identified and measured R_e is 2.3 Ω, and the one of L_e is 0.70 μH. So, the proposed method can achieve high accuracy on the condition of phase-shift angle variation.

Furthermore, the influences of different order harmonics are analyzed. As shown in Fig. 5, the WPT harmonics can be divided into two parts: the primary-side and secondary-side harmonics. As suggested by (16) and (17), the primary-side harmonics

TABLE IV
HARMONIC ACTIVE POWERS OF INVERTER OUTPUT USED FOR IDENTIFICATION ON THE CONDITION OF DIFFERENT PHASE-SHIFT ANGLES

Phase Shift Angle	Harmonic Active Power of Inverter Output (W)		
α (Degree)	3 Order Harmonics	5 Order Harmonics	7 Order Harmonics
0	0.091	0.011	0.003
20	0.069	0.005	≈ 0
40	0.023	≈ 0	0.002
60	≈ 0	0.008	0.002

TABLE V
FUNDAMENTAL AND HARMONIC RECTIFIER INPUT CURRENTS USED FOR IDENTIFICATION ON THE CONDITION OF DIFFERENT BATTERY VOLTAGES

Experimental Battery Voltage	Rectifier Input Current Amplitude (A)			
U_b (V)	Fundamental Wave	3 Order Harmonics	5 Order Harmonics	7 Order Harmonics
300	12.40	1.04	0.36	0.18
320	11.76	1.08	0.37	0.19
340	10.74	1.15	0.39	0.20
360	9.48	1.22	0.42	0.21

mainly affect the proposed method through the harmonic active power of the inverter output. Hence, the harmonic inverter output active powers, which is used to obtain the experimental identification results, are given in Table IV, on the condition of different phase-shift angles. It suggests that the powers of three-, five-, and seven-order harmonics are all very small compared with the power level of the developed WPT prototype. So, their effects can be neglected to simplify the parameter relationship and identification process.

Meanwhile, the secondary-side harmonics mainly influence the proposed method through harmonic rectifier input currents, as suggested by (21). This will affect I_b identification results. So, the fundamental and harmonic rectifier input currents, which is used to obtain the experimental identification results, are given in Table V. It suggests that the amplitudes of the harmonic rectifier input currents decrease with the harmonic order. This means the harmonic effect will reduce when its order increases. Also, the harmonic current amplitudes are not significantly smaller than the fundamental ones, especially for the three-order harmonic. Therefore, their effects cannot be neglected when getting the experimental I_b identification results.

Finally, the case of coil misalignment is discussed and the results are shown in Fig. 13, where the measured mutual inductance M is 19.81 μH when the coils have 15 cm lateral misalignment, and then this M value is updated to get the experimental identification results. Further calculations indicate that the maximum identification errors of R_L, U_b, and I_b are 4.2%, 3.5%, and 2.2%, respectively, while the maximum difference between the identified and measured R_e is 4.3 Ω, and the one of L_e is 2.1 μH. Compared with the coil alignment condition, the deviations are relatively bigger here. This is mainly due to the effects of coil self-inductance slight changes, which are not updated during the implementation of the method. These errors are relatively bigger but still acceptable, which means the proposed method is also

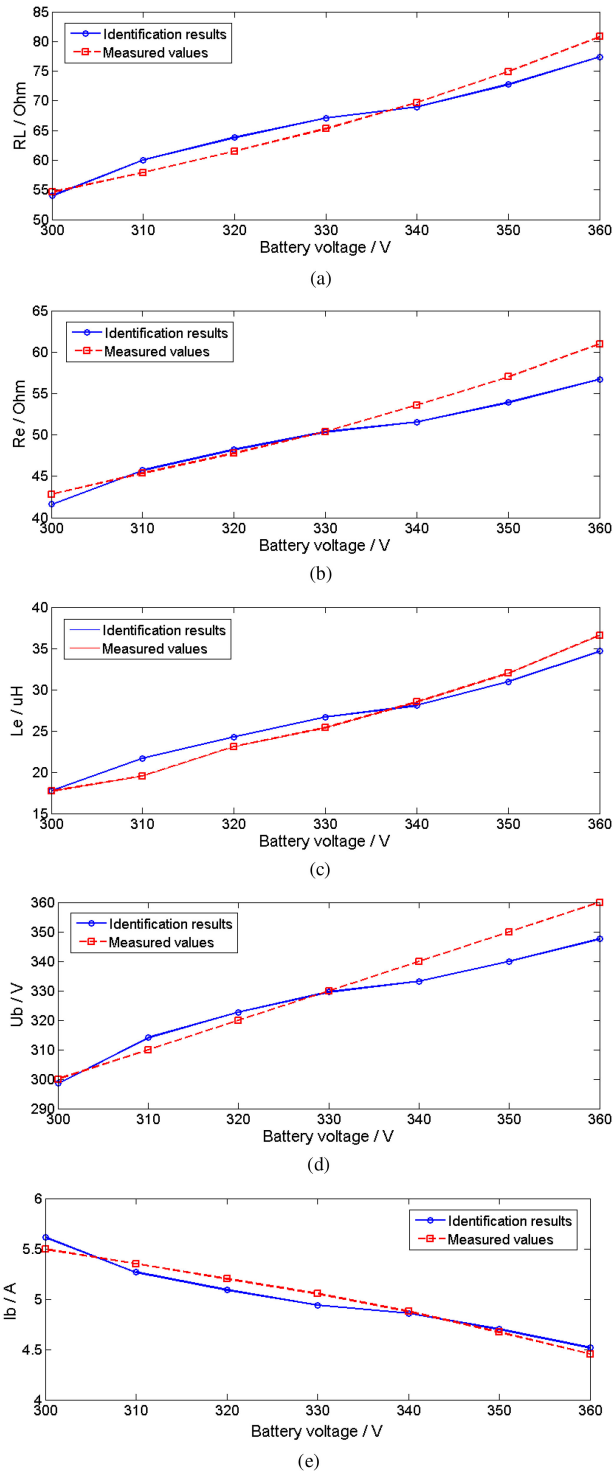

Fig. 13. Load parameter identification results when the coils have 15 cm misalignment. (a) R_L identification results. (b) R_e identification results. (c) L_e identification results. (d) U_b identification results. (e) I_b identification results.

suitable for the coil misalignment condition. Additionally, a little higher accuracy can be achieved compared with the existing load resistance identification methods (the maximum experimental error of the load resistance identification is 5.6% in [6], the maximum simulation error of the load resistance identification is 7.9% in [8], and the maximum experimental error of the load resistance identification is less than 5.2% in [35]). Further work will be focused on reducing the identification errors and improving the robustness to minimize the effects of the system parameter variations as well as adopting the proposed method to achieve the WPT system control.

V. Conclusion

This article presents a WPT load parameter identification method using only the dc input current and phase-shift angle. It can achieve the joint identification of battery voltage, equivalent resistance, charging current, and WPT equivalent load impedance with high accuracy. Based on the proposed fundamental–harmonic model and the developed WPT prototype, the following main conclusions are obtained: WPT variables and characteristics can be precisely studied, adopting the presented linear superposition analysis of the system fundamental wave and harmonics; the proposed multiple load parameter joint identification method can achieve relatively high accuracy on the conditions of battery voltage change, phase-shift angle variation, and coil misalignment. These works will lay a foundation for control strategy investigation, system performance improvement, and condition monitoring based on the load parameter identification.

References

[1] G. A. Covic and J. T. Boys, "Modern trends in inductive power transfer for transportation applications," *IEEE J. Emerg. Sel. Topics Power Electron.*, vol. 1, no. 1, pp. 28–41, Mar. 2013.

[2] S. Y. R. Hui, W. X. Zhong, and C. K. Lee, "A critical review of recent progress in mid-range wireless power transfer," *IEEE Trans. Power Electron.*, vol. 29, no. 9, pp. 4500–4511, Sep. 2014.

[3] C. C. Mi, G. Buja, S. Y. Choi, and C. T. Rim, "Modern advances in wireless power transfer systems for roadway powered electric vehicles," *IEEE Trans. Ind. Electron.*, vol. 63, no. 10, pp. 6533–6545, Oct. 2016.

[4] Z. Zhang, H. Pang, A. Georgiadis, and C. Cecati, "Wireless power transfer—An overview," *IEEE Trans. Ind. Electron.*, vol. 66, no. 2, pp. 1044–1058, Feb. 2019.

[5] J. Yin, D. Lin, T. Parisini, and S. Y. R. Hui, "Front-end monitoring of the mutual inductance and load resistance in a series–series compensated wireless power transfer system," *IEEE Trans. Power Electron.*, vol. 31, no. 10, pp. 7339–7352, Oct. 2016.

[6] Y.-G. Su, L. Chen, X.-Y. Wu, A. P. Hu, C.-S. Tang, and X. Dai, "Load and mutual inductance identification from the primary side of inductive power transfer system with parallel-tuned secondary power pickup," *IEEE Trans. Power Electron.*, vol. 33, no. 11, pp. 9952–9962, Nov. 2018.

[7] J. Yin, D. Lin, C.-K. Lee, and S. Y. R. Hui, "A systematic approach for load monitoring and power control in wireless power transfer systems without any direct output measurement," *IEEE Trans. Power Electron.*, vol. 30, no. 3, pp. 1657–1667, Mar. 2015.

[8] K. Song, Z. J. Li, J. H. Jiang, and C. Zhu, "Constant current/voltage charging operation for series–series and series–parallel compensated wireless power transfer systems employing primary-side controller," *IEEE Trans. Power Electron.*, vol. 33, no. 9, pp. 8065–8080, Sep. 2018.

[9] X. Dai, X. Li, Y. Li, and A. P. Hu, "Maximum efficiency tracking for wireless power transfer systems with dynamic coupling coefficient estimation," *IEEE Trans. Power Electron.*, vol. 33, no. 6, pp. 5005–5015, Jun. 2018.

[10] J. Kim *et al.*, "Coil design and shielding methods for a magnetic resonant wireless power transfer system," *Proc. IEEE*, vol. 101, no. 6, pp. 1332–1342, Jun. 2013.

[11] Y. Wang, Y. Yao, X. Liu, D. Xu, and L. Cai, "An LC/S compensation topology and coil design technique for wireless power transfer," *IEEE Trans. Power Electron.*, vol. 33, no. 3, pp. 2007–2025, Mar. 2018.

[12] S. Li, W. Li, J. Deng, T. D. Nguyen, and C. C. Mi, "A double-sided LCC compensation network and its tuning method for wireless power transfer," *IEEE Trans. Veh. Technol.*, vol. 64, no. 6, pp. 2261–2273, Jun. 2015.

[13] Y. Yao, Y. Wang, X. Liu, F. Lin, and D. Xu, "A novel parameter tuning method for a double-sided LCL compensated WPT system with better comprehensive performance," *IEEE Trans. Power Electron.*, vol. 33, no. 10, pp. 8525–8536, Oct. 2018.
[14] J.-G. Kim, G. Wei, M.-H. Kim, J.-Y. Jong, and C. Zhu, "A comprehensive study on composite resonant circuit-based wireless power transfer systems," *IEEE Trans. Ind. Electron.*, vol. 65, no. 6, pp. 4670–4680, Jun. 2018.
[15] M. Dionigi, M. Mongiardo, and R. Perfetti, "Rigorous network and full-wave electromagnetic modeling of wireless power transfer links," *IEEE Trans. Microw. Theory Techn.*, vol. 63, no. 1, pp. 65–75, Jan. 2015.
[16] Y. Guo, L. Wang, Y. Zhang, S. Li, and C. Liao, "Rectifier load analysis for electric vehicle wireless charging system," *IEEE Trans. Ind. Electron.*, vol. 65, no. 9, pp. 6970–6982, Sep. 2018.
[17] S. Samanta and A. K. Rathore, "A new inductive power transfer topology using direct ac–ac converter with active source current waveshaping," *IEEE Trans. Power Electron.*, vol. 33, no. 7, pp. 5565–5577, Jul. 2018.
[18] B. H. Choi, E. S. Lee, J. Huh, and C. T. Rim, "Lumped impedance transformers for compact and robust coupled magnetic resonance systems," *IEEE Trans. Power Electron.*, vol. 30, no. 11, pp. 6046–6056, Nov. 2015.
[19] Y. Zhou, W. Lin, and B. Wang, "High-efficiency coupling-insensitive wireless power and information transmission based on the phase-shifted control," *IEEE Trans. Power Electron.*, vol. 33, no. 9, pp. 7821–7831, Sep. 2018.
[20] Y. Fang and B. M. H. Pong, "Multiple harmonics analysis for variable frequency asymmetrical pulsewidth-modulated wireless power transfer systems," *IEEE Trans. Ind. Electron.*, vol. 66, no. 5, pp. 4023–4030, May 2019.
[21] Y. Chen, W. Xiao, Z. Guan, B. Zhang, D. Qiu, and M. Wu, "Nonlinear modeling and harmonic analysis of magnetic resonant WPT system based on equivalent small parameter method," *IEEE Trans. Ind. Electron.*, vol. 66, no. 8, pp. 6604–6612, Aug. 2019.
[22] Y. Zhang, T. Kan, Z. Yan, Y. Mao, Z. Wu, and C. C. Mi, "Modeling and analysis of series-none compensation for wireless power transfer systems with a strong coupling," *IEEE Trans. Power Electron.*, vol. 34, no. 2, pp. 1209–1215, Feb. 2019.
[23] R. Mai, Y. Liu, Y. Li, P. Yue, G. Cao, and Z. He, "An active-rectifier-based maximum efficiency tracking method using an additional measurement coil for wireless power transfer," *IEEE Trans. Power Electron.*, vol. 33, no. 1, pp. 716–728, Jan. 2018.
[24] H. Li, K. Wang, L. Huang, W. Chen, and X. Yang, "Dynamic modeling based on coupled modes for wireless power transfer systems," *IEEE Trans. Power Electron.*, vol. 30, no. 11, pp. 6245–6253, Nov. 2015.
[25] J. P.-W. Chow, H. S.-H. Chung, and C.-S. Cheng, "Use of transmitter-side electrical information to estimate mutual inductance and regulate receiver-side power in wireless inductive link," *IEEE Trans. Power Electron.*, vol. 31, no. 9, pp. 6079–6091, Sep. 2016.
[26] K. Leslie, I. Demirkiran, E. Rask, and H. Lohse-Busch, "An investigation into the PNGV battery model with the addition of a dynamic temperature range," in *Proc. IEEE Southeastcon*, 2013, pp. 1–6.
[27] Z. Zhang, X. Cheng, Z.-Y. Lu, and D.-J. Gu, "SOC estimation of lithium-ion battery pack considering balancing current," *IEEE Trans. Power Electron.*, vol. 33, no. 3, pp. 2216–2226, Mar. 2018.
[28] Y. Jiang, L. Wang, Y. Wang, J. Liu, M. Wu, and G. Ning, "Analysis, design, and implementation of WPT system for EV's battery charging based on optimal operation frequency range," *IEEE Trans. Power Electron.*, vol. 34, no. 7, pp. 6890–6905, Jul. 2019.
[29] H. Feng, T. Cai, S. Duan, X. Zhang, H. Hu, and J. Niu, "A dual-side-detuned series–series compensated resonant converter for wide charging region in a wireless power transfer system," *IEEE Trans. Ind. Electron.*, vol. 65, no. 3, pp. 2177–2188, Mar. 2018.
[30] M. Kim, D.-M. Joo, and B. K. Lee, "Design and control of inductive power transfer system for electric vehicles considering wide variation of output voltage and coupling coefficient," *IEEE Trans. Power Electron.*, vol. 34, no. 2, pp. 1197–1208, Feb. 2019.
[31] D.-H. Kim and D. Ahn, "Self-tuning LCC inverter using PWM-controlled switched capacitor for inductive wireless power transfer," *IEEE Trans. Ind. Electron.*, vol. 66, no. 5, pp. 3983–3992, May 2019.
[32] J. Hou, Q. Chen, Z. Zhang, S.-C. Wong, and C. K. Tse, "Analysis of output current characteristics for higher order primary compensation in inductive power transfer systems," *IEEE Trans. Power Electron.*, vol. 33, no. 8, pp. 6807–6821, Aug. 2018.
[33] Q. Zhao, A. Wang, J. Liu, and X. Wang, "The load estimation and power tracking integrated control strategy for dual-sides controlled LCC compensated wireless charging system," *IEEE Access*, vol. 7, pp. 75749–75761, 2019.
[34] X. Meng, D. Qiu, M. Lin, S. C. Tang, and B. Zhang, "Output voltage identification based on transmitting side information for implantable wireless power transfer system," *IEEE Access*, vol. 7, pp. 2938–2946, 2019.
[35] S. Liu, X. Li, and L. Yang, "Three-coil structure-based WPT system design for electric bike CC and CV charging without communication," *IET Electr. Power Appl.*, vol. 13, no. 9, pp. 1318–1327, Sep. 2019.

Yanjie Guo received the Ph.D. degree in electrical engineering from the Institute of Electrical Engineering, Chinese Academy of Sciences, Beijing, China, in 2013.

He is currently an Associate Professor with the Key Laboratory of Power Electronics and Electric Drives, Chinese Academy of Sciences, Beijing, and also with the University of Chinese Academy of Sciences, Beijing, China. His research interests include wireless power transfer, stationary and dynamic wireless charging systems for electric vehicles, power electronics converters and control, battery management, and electromagnetic compatibility.

Yuwang Zhang received the Ph.D. degree in electrical engineering from the Institute of Electrical Engineering, Chinese Academy of Sciences (IEECAS), Beijing, China, in 2020.

He is currently a Postdoctoral Researcher with the Department of Vehicle Energy System and Control Technology, IEECAS, Beijing. His research interests include wireless power transfer theory, optimization and control of electric vehicle wireless charging system, and bidirectional wireless charging system.

Shufan Li received the M.S. degree in electrical engineering from the University of Chinese Academy of Sciences, Beijing, China, in 2016. He is currently working toward the Ph.D. degree in electrical engineering with the Institute of Electrical Engineering, Chinese Academy of Sciences, Beijing, China.

His research interests include wireless power transfer theory, parameter estimation and control, and dynamic EV wireless charging systems.

Chengxuan Tao (Member, IEEE) received the M.S. degree in control science and engineering from Chongqing University, Chongqing, China, in 2012. He is currently working toward the Ph.D. degree in mechanical engineering with the Beijing Institute of Technology, Beijing, China.

Since 2012, he has been with the Institute of Electrical Engineering, Chinese Academy of Sciences, Beijing, China, where he is currently an Engineer. His research interests include circuit topology, analysis, and control of wireless power transfer system, especially its applications in special fields.

Lifang Wang (Member, IEEE) received the Ph.D. degree in automotive engineering from Jilin University, Changchun, China, in 1997.

She joined the Institute of Electrical Engineering, Chinese Academy of Sciences (IEECAS), Beijing, China, where she is currently the Director of the Department of Vehicle Energy System and Control Technology. She is also the Vice Director of the Key Laboratory of Power Electronics and Electric Drives, Chinese Academy of Sciences, Beijing, China. During the Chinese tenth-five year plan (2001–2005), she was a member of the National Specialist Group of Key Special Electric Vehicle Project of the National 863 Program, and she was the Head of the 863 Special EV Project Office. Her research interests include wireless charging system for EV, EV control system, EV battery management system, electromagnetic compatibility, and smart electricity use.